Research Article
Vol. 27, No. 14 | 8 Jul 2019 | OPTICS EXPRESS 19788
Optics EXPRESS

Encoding of arbitrary micrometric complex illumination patterns with reduced speckle

MIGUEL CARBONELL-LEAL, GLADYS MÍNGUEZ-VEGA, JESÚS LANCIS, AND OMEL MENDOZA-YERO*

Institut de Noves Tecnologies de la Imatge (INIT), Universitat Jaume I, 12080 Castelló, Spain
**omendoza@fca.uji.es*

Abstract: In nonlinear microscopy, phase-only spatial light modulators (SLMs) allow achieving simultaneous two-photon excitation and fluorescence emission from specific region-of-interests (ROIs). However, as iterative Fourier transform algorithms (IFTAs) can only approximate the illumination of selected ROIs, both image formation and/or signal acquisition can be largely affected by the spatial irregularities of the illumination patterns and the speckle noise. To overcome these limitations, we propose an alternative complex illumination method (CIM) able to generate simultaneous excitation of large-area ROIs with full control over the amplitude and phase of light and reduced speckle. As a proof-of-concept we experimentally demonstrate single-photon and second harmonic generation (SHG) with structured illumination over large-area ROIs.

1. Introduction

In some recent introduced multiphoton microscopy techniques, simultaneous excitation and signal collection from multiple specific cell populations have become into key tools for monitoring the cellular activity [1–3]. This basically happens because multiple millisecond time response signals e.g., fluorescence-lifetime signals, produced by many cellular ensembles cannot be acquired by means of conventional scanning methods. For instance, in point by point scanning methods the temporal resolution is limited by the signal-to noise ratio, which is close-related to the pixel dwell time. That is, the longer the pixel dwell time, the higher the signal-to-noise ratio but consequently, temporal resolution gets worse. An alternative illumination technique employed to reduce the acquisition time relies on the parallel excitation of the cellular targets by using multifocal irradiance patterns. On this topic, multifocal multiphoton microscopy can be carried out by several methods including, but not limited to, the use of microlens arrays [4,5], beam splitting [6], or Fresnel holograms [7]. However, it is apparent that multifocal illumination allows us to excite only focal-size sites in the cells, which certainly limits the acquired information e.g., voltage signals, to those focal regions determined by the spatial features of the excitation foci.

On the other hand, the combination of wide-field illumination techniques with high-sensitivity cameras (e.g., TE-cooled, ultra-sensitive photon detecting, electron multiplying charge-coupled camera) can be regarded as a prominent solution to simultaneously excite and collect not just from focal-size sites within the cells, but also from large-area ROIs of them. In this case all ROIs of the biological cells delimited by the numerical aperture of the objective could be turned into single-photon fluorescence signals, although it is less likely to induce multiphoton absorption and fluorescence emission due to both the exponential intensity requirements of nonlinear processes and the spreading of the laser power over the extended regions. Hence, instead of conventional mode locked Ti: sapphire laser oscillators, additional chirped pulse amplification stages with average power capabilities up to several watts and repetition rates of tens of kHz become better candidates of choice for performing wide-field multiphoton microscopy [8,9].

#365662 https://doi.org/10.1364/OE.27.019788
Journal © 2019 Received 22 Apr 2019; revised 13 Jun 2019; accepted 18 Jun 2019; published 1 Jul 2019

Optics EXPRESS

In this context, commercially available SLMs have allowed for simultaneous excitation of several ROIs within a cellular ensemble thanks to a proper optical manipulation of ultrashort laser pulses [2,10–20]. Here, if one takes a look at the wide variety of reported illumination methods, those ones based on the use of phase-only SLMs seems to stand out because of their potential to manage light with relatively high throughputs. In particular, wide-field nonlinear excitation has been experimentally demonstrated by the coherent reconstruction of computer-generated holograms (CGHs) at the sample plane. In this case, although long part of the available energy can be transferred to specific ROIs within the cellular ensemble, there still exist several problems to face out. For instance, unwanted effects like angular dispersion or chromatic aberrations may cause spatiotemporal distortions of the reconstructed hologram, which clearly decrease the signal-to-noise ratio and harm the quality of the obtained cell image. In addition, the coherent noise (speckle) associated with the superposition of coherent light with different path lengths prevents wide-field excitation based on CGHs to be well-accomplished over other ROIs different than the line-shaped illumination regions typically reported in the literature [7,10]. Therefore, under coherent illumination, the reconstruction of CGHs is currently unable to generate spatially homogeneous irradiance patterns over ROIs with dimensions on the order of the typical cellular-sizes, not to mention its inefficiency to precisely manipulate the amount of energy put into them e.g., to generate multiple-intensity level illumination patterns. At this point, improved versions of the well-known Gerchberg-Saxton algorithm [21] have allowed both speckle reduction and phase control of 1-D illumination patterns [11,22]. In addition, some recently reported CGH-based methods can generate controllable illumination patterns with multiple energy levels, but without phase control [23]. So, as far as we known, there is no report on the utilization of proper 2-D illumination methods that give us high accuracy and complete control over the amplitude and phase of the light without speckle noise.

In this manuscript we propose an interferometric CIM able to induce linear and nonlinear excitation of multiple cellular-size ROIs with full and independent control over the amplitude and phase of the light at the sample plane. Its ability to precisely modify the complex field of the spatially coherent light emitted by a femtosecond laser is experimentally shown to be crucial to obtain not only homogenous irradiance patterns (without speckle) over different ROIs, but also multiple-intensity levels with arbitrary phase content in all cases. To show the usefulness of our method to generate controllable light patterns, we experimentally demonstrate single photon illumination/excitation of a certain micrometric ROI by using different predefined complex field patterns. In addition, another proof-of-concept experiment, this time addressed to induce SHG of a specific ROI within a Type 1 $\beta - BaB_2O_4$ (BBO) crystal is also shown. All optical control of the illumination patterns is carried out with a single phase element implemented into a phase-only SLM. The phase element is computer generated by using a complex field encoding method based on double-phase hologram theory that was previously reported [12]. Some results achieved with our CIM were compared with similar ones obtained by the reconstruction of CGHs.

2. Basics of the complex illumination method

In this section we introduce the theory underlying the CIM. The corresponding setup is basically composed of two consecutive optical modules that we refer throughout the whole manuscript as complex field encoding module (CFEM) and optical demagnifying module (ODM), respectively, see Fig. 1.

When the light passes through the CFEM, its optical wavefront is properly phase modulated to get user-defined complex fields at the output plane. In accordance with the theory [12], any two-dimensional complex field expressed in the form $U(x,y) = A(x,y)e^{i\varphi(x,y)}$, where $A(x,y)$ and $\varphi(x,y)$ hold for the amplitude and phase functions, respectively, can be rewritten as:

Optics EXPRESS

$$U(x,y) = Be^{i\theta(x,y)} + Be^{i\vartheta(x,y)}. \quad (1)$$

In Eq. (1), $B = A_{\max}/2$ is an amplitude constant term (it does not depends on the transversal coordinates x, y), $A_{\max}$ is the maximum value of $A(x,y)$, and the new phase functions $\theta(x,y)$ and $\vartheta(x,y)$ can be calculated from $A(x,y)$ and $\varphi(x,y)$ by using the expressions:

$$\theta(x,y) = \varphi(x,y) + \cos^{-1}[\mathrm{A(x,y)} / \mathrm{A}_{\max}]. \quad (2)$$

$$\vartheta(x,y) = \varphi(x,y) - \cos^{-1}\left[A(x,y)/A_{\max}\right]. \quad (3)$$

From a physical point of view (for $A_{\max} = 2$), Eqs. (1-3) mean that the complex field $U(x,y)$ can be retrieved from the coherent interference of the two uniform waves $e^{i\theta(x,y)}$ and $e^{i\vartheta(x,y)}$. Such interference can be carried out by means of a common-path interferometer made up of a spatially filtered 4f optical system. The screen of a phase-only SLM is placed at the input plane of the CFEM, and the following phase element $\alpha(x,y)$ is implemented on the SLM

$$\alpha(x,y) = M_1(x,y)\theta(x,y) + M_2(x,y)\vartheta(x,y). \quad (4)$$

The phase element $\alpha(x,y)$ is derived from the transversal spatial mapping of $e^{i\theta(x,y)}$ and $e^{i\vartheta(x,y)}$ with two-dimensional binary gratings $M_1(x,y)$ and $M_2(x,y)$ (checkerboard patterns) taken at the Nyquist limit, that is

$$M_1(x,y)e^{i\theta(x,y)} + M_2(x,y)e^{i\vartheta(x,y)} = e^{i\alpha(x,y)}. \quad (5)$$

The checkerboard patterns fulfill the complementary condition $M_1(x,y) + M_2(x,y) = 1$. Here, it should be noted that, by itself, send the phase element $\alpha(x,y)$ to the SLM does not guaranties the interference of both uniform waves. This is carried out by means of a suited spatial filter placed at the Fourier plane of the imaging system. It can be shown that if we use a filter to block all diffraction orders but the zero one, we are able to exactly retrieve the full spectrum of the original complex field at the Fourier plane [12]. Consequently, at the output plane of the CFEM we find the convolution of the magnified spatially reversed complex field with the Fourier transform of the filter. It means that full amplitude and phase information of the complex field can be retrieved at the output plane, except for a certain loss of spatial resolution due to the convolution operation.

On the other hand, the ODM allows us to proper rescale, onto the sample plane, the complex field generated at the output plane of the CFEM. The ODM is composed of a refractive achromatic lens with long-distance focal length and an infinity corrected microscope objective, which generate a demagnified image of the reconstructed complex field onto the sample plane. In Fig. 1, the whole optical setup corresponding to the CIM is shown.

3. Single photon experiments

To demonstrate, as a proof-of-concept, the ability of the method to generate arbitrary complex illumination patterns at micrometric scale, we carried out several single photon experiments. The employed optical setup is shown in Fig. 1. Ultrashort pulses emitted by a Ti: Sapphire amplifier laser (30 fs amplitude full-width at half maximum (FWHM), central wavelength 800 nm, bandwidth of 50 nm FWHM, maximum energy per pulse of 0.8 mJ, and 1 kHz repetition rate) are employed as a light source. The SLM (HOLOEYE PLUTO, resolution 1920x1080, and pixel pitch 8 μm) used in our experiments was previously calibrated [24] for a significant set of frequency components of the light pulse with the help of three bandpass filters of 10 nm FWHM. The similar phase response curves (calibration curves) obtained for the three different spectral lines allow performing wavefront modulation of ultrashort pulses with a single phase element $\alpha(x,y)$. In addition, to mitigate the effect of abrupt spatial variations in the phase

Optics EXPRESS

modulation [25] (pixel crosstalk effects), the two-dimensional binary gratings $M_1(x, y)$ and $M_2(x, y)$ were constructed with 4x4 pixel-cells.

In the optical setup shown in Fig. 1, the light is sent to the SLM by using silver mirrors and reflected from them forming a small angle (about 3 degrees) with respect to the normal incidence. In these conditions, the desired complex field $U(x, y)$ is reconstructed at the output plane of the CFEM. The CFEM is made up of a couple refractive lenses (L_1 and L_2) with focal lengths L_1 = 1000 mm and L_2 = 500 mm, which result in a transversal magnification of ½ at its output plane. In addition, a circular iris is placed at the Fourier plane to filter all diffraction orders but the zero one. Finally, the ODM allows the complex field illumination $U(x, y)$ to be imaged into the sample plane.

A rough coupling between the size of the illumination pattern and that of the sample is carried out with a proper selection of optical components of the ODM. In our experiment, it is made up of an achromatic lens (L_3) of focal length 400 mm and a 20x infinity-corrected microscope objective (MO_1), which led to a total demagnification of about 1/73 at the sample plane. The transmitted light is collected with the help of a 50x infinity-corrected microscope objective (MO_2) and sent to a CCD camera (Basler avA1600-50gm), where the image of the sample is recorded (see Fig. 1). To adjust the intensity of the light at the sample plane a set of broadband neutral filters was employed. A more accurate selection of the illumination zone over the sample is done later once the specific ROIs are defined. At this point it is possible to establish the main features of the illumination pattern $U(x, y)$. For instance, its amplitude function $A(x, y)$ can be set by means of a multilevel spatial energy distribution, or its phase function $\varphi(x, y)$ by using a proper phase distribution to compensate for specimen-induced or microscope objective spherical aberrations.

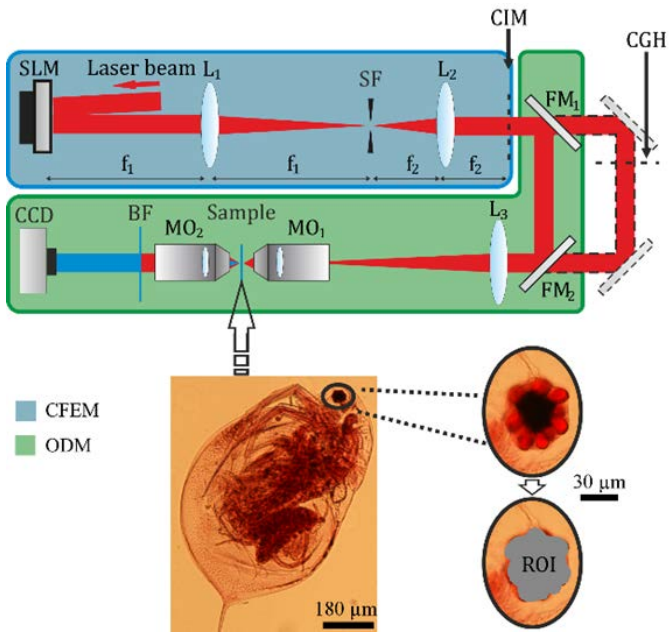

Fig. 1. Optical setup. Complex illumination method (CIM) implemented by means of two optical modules: complex field encoding module (CFEM, blue region) used to generate the arbitrary complex patterns, and optical demagnifying module (ODM, green region) used to adjust the size of the pattern at the sample plane. In order to properly set the position of the utilized CGHs, a delay line is added at the right part of the setup. Bottom part shows an image of the biological specimen (water flea) used to define a ROI.

Optics EXPRESS

In Fig. 2, an example of a complex illumination pattern is shown. In this case, we simulate a ROI within a Daphnia specimen (water flea) that coincides with its eye. Note that, such ROI has approximate dimensions of 60x60 μm^2. The complex field given in top part of Fig. 2 is characterized by an amplitude pattern having four different energy levels distributed among quadrants within the eye, whereas its spatial phase is given by the analytical function $\varphi(x,y) = \pi/2 \sin\left[2\pi x/(5\lambda)\right]\cos\left[2\pi y/(5\lambda)\right]$. From the above-defined amplitude and phase parameters we can calculate the phase element $\alpha(x,y)$ used to reconstruct the expected complex field. To do that, we follow the procedure described in section 2, also represented schematically in central part of Fig. 2. Here, to clearly see the roll of sampling gratings $M_1(x,y)$ and $M_2(x,y)$ on this procedure, the phase element $\alpha(x,y)$ was represented with pixel-cells of 60x60. Polarization-based phase shifting technique [26] is applied to measure the amplitude and phase of the complex illumination pattern at the sample plane. This phase shifting technique can be accomplished by simple addition of a couple of polarization-dependent optical elements e.g., two polarizers. Specifically, a broadband halfwave plate (EKSMA OPTICS 460-4215) was placed before the SLM plane to rotate the original direction of polarization of all frequency components of the ultrashort pulse 45 degrees with respect to the SLM director orientation. This allows only part of the incident light to be phase modulated (object beam), while the remaining one (reference beam) is not diffracted. In order to generate four different phase shifting interferograms at the sample plane, uniform phases with steps of π/2 radians were added to the phase element $\alpha(x,y)$. The interferograms are formed after recombining both reference and object beams with the help of a broadband linear polarizer (EKSMA OPTICS 420 0526M), this time located before the 20x microscope objective MO_1. In practice, the position of the rotational angle with respect to SLM director orientation determines the amount of diffracted and non-diffracted light within the interferograms. In the bottom-central part of Fig. 2, the interferograms measured for the phase steps 0, π/2, π, and 3π/2 are shown. These interferograms were recorded without moving the position of the camera in the optical setup. The experimental amplitude and phase patterns determined from the above phase shifting interferograms are given in the bottom part of Fig. 2. It is apparent that experimental results are in good agreement with the theory. However, as it might be expected due to the convolution operation (see section 2) and the used pixel-cell, the spatial resolution of recorded amplitude and phase patterns is a few pixels lower than corresponding theoretical ones. Even so, the root-mean-square error (RMSE) between theory and experiment yields discrepancies of 6.8% and 14% for amplitude and phase images, respectively.

Now, we test the usefulness of the CIM to synthetize amplitude-only irradiance patterns at micrometric scale. On one side, we are interested in the generation of spatially uniform irradiance patterns for simultaneous wide-field illumination. Note that the excitation of extended ROIs with non-uniform irradiance patterns may cause image blurring due to different signal responses of similar biological components. In wide-field two-photon microscopy this is crucial because the recorded signal depends on the square of the light intensity. In other cases, simultaneous excitation of extended ROIs (not by multifocal excitation) through beam shaping of coherent radiation cannot be accomplished without coherent noise (speckle).

Optics EXPRESS

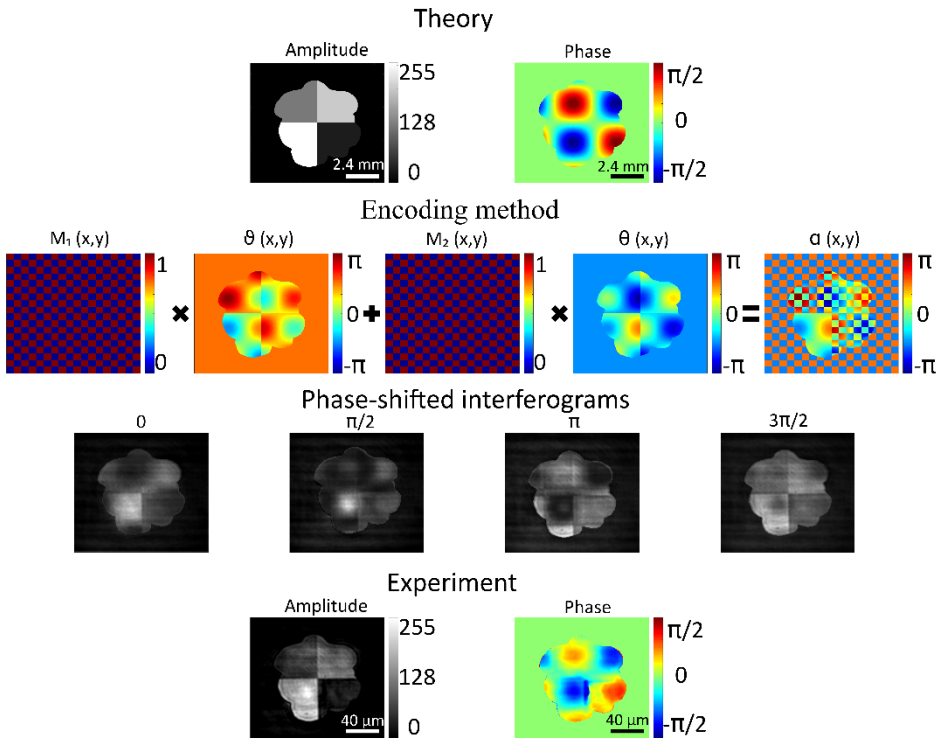

Fig. 2. Generic example: measured amplitude and phase of a given complex field at the SLM (top) and sample (bottom) planes. Related CIM images and measured interferograms are also shown (central part). Scales are included as insets at the right-bottom part of each irradiance pattern.

In contrast, by applying the proposed CIM we obtain spatial uniform illumination of extended ROIs without speckle (please, see top-right part of Fig. 3). In this experiment, as before, we select a ROI whose shape is determined by the borders of the Daphnia 'eye. The first column of Fig. 3 shows the phase elements $\alpha(x, y)$ represented with a pixel-cell of 6x6. Here, the RMSE between theory and experiment yields discrepancies of 7%. The spatial uniformity of the recorded pattern mainly depends on the spatial profile of the laser beam at the SLM plane, and also to a lesser extent, of optical irregularities (scratches in mirrors or lenses, unwanted dust on the surface of optical components, etc.). Furthermore, as this irradiance pattern is basically constructed by conjugating the SLM plane with the sample plane, measured irradiance patterns are free from coherent noise.

On the other side, we push the CIM to the limit by implementing irradiance patterns with multiple energy levels and complex spatial structure. To this end, we reproduce inside of the ROI given by the Daphnia's eye (about 60x60 μm^2 only) a mushroom image. After a visual comparison of results shown in Fig. 3, one can realize that the recorded irradiance pattern reproduces very well the expected one. In fact, we are able to spatially resolve image details in the sample plane of the order of 5 μm i.e., the white spots. Here, it should mentioned that the minimum feature size of our system is about 0.87 μm. In this case, the RMSE between theory and experiment yields discrepancies of 10%. With this experiment, we want to show the potential of the CIM to manage different energy levels of excitation simultaneously. It is apparent that different constituents of cells and/or fluorophores might imply different excitation thresholds. So, in principle, one can think in setting energy-custom illumination patterns depending on the nature of the biological sample. Additionally, this fine control over

Optics EXPRESS

the energy content of the illumination pattern can be also useful to adjust the energy levels over the whole sample without the necessity of using neutral filters.

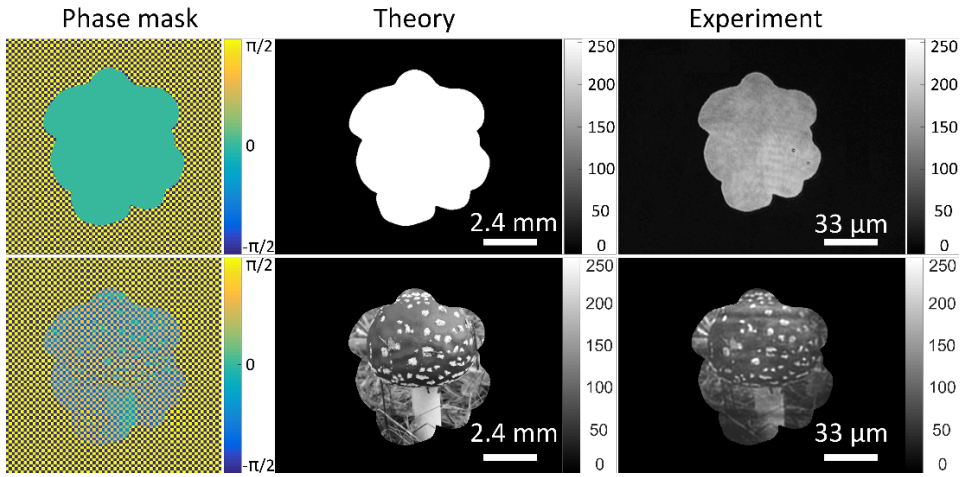

Fig. 3. Theoretical and experimental amplitude-only irradiance patterns at the SLM and sample planes, respectively. Scales are included as insets at the right-bottom part of each irradiance pattern. In the first column, corresponding phase elements, represented with a pixel cell of 6x6, are also shown.

In order to highlight the role of the phase in practical tasks we carried out real optical aberration corrections using the CIM. For this purpose, we constructed and introduced a Michelson interferometer within the CFEM to measure the phase. In this setup, the light impinges perpendicular to the liquid crystal display after being divided into two similar beamlets with a broadband beam splitter. In the first arm of the interferometer, the light (object beam) goes to the SLM and is reflected back to the CFEM via beam splitter, whereas in the second arm, the light (reference beam) follows a similar optical path, but is reflected by a silver mirror. This mirror can be slightly moved (delay line) to adjust the path length of both arms. The phase is measured at the output plane of the CFEM by applying the Polarization-based phase shifting technique [26] in a similar manner as described before. However, in contrast to previously common-path setup, this type of interferometer is able to determine the optical aberrations of the optical system. The conjugated measured phase is encoded with the CIM algorithm to get both significant correction for optical aberrations and synthesis of desired complex field, simultaneously.

In Fig. 4 some specific results are shown. In the simplest example, a complex field made up of a uniform amplitude and a flat phase is encoded into the SLM, see Fig. 4(a). The amplitude pattern, given by the borders of Daphnia's eye, and shown as an inset in the left-bottom part of each image, is the same in all cases. Although the encoded phase is flat, in practice the retrieved phase from the phase shifting interferograms shows clear optical aberrations, see Fig. 4(b). These aberrations can be largely compensated if we take them into account within the CIM algorithm, as shown in Fig. 4(c). To do that, it is sufficient to encode the conjugated of the measured optical aberrations together with the complex pattern. This aberration correction task is usually necessary to better approach the reconstructed complex field to the expected one. Last example shown in Fig. 4(d)-(f) illustrates this situation. In this case, the desired phase pattern is originally given in Fig. 4(d), whereas the real retrieved phase is distorted by optical aberrations, see Fig. 4(e). By using the CIM we can correct most optical aberrations, achieving the phase pattern given in Fig. 4(f), which is closer to the desired one.

Optics EXPRESS

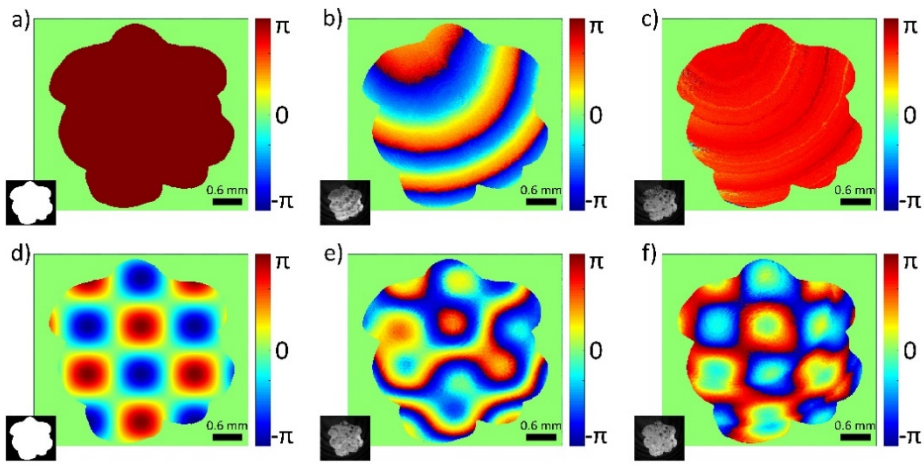

Fig. 4. Two examples of compensation for real optical aberrations with the CIM. The measured amplitude patterns are included as insets at the left-bottom parts of each image.

In most aberration compensation techniques based on a phase-only SLM, the liquid crystal display is used just to implement the necessary conjugated phase to compensate for previously measured optical aberrations. In contrast, the encoding algorithm associated with the CIM allows us to perform wavefront correction and manipulate the amplitude of the complex field, simultaneously.

4. Non-linear excitation experiment

In this section we experimentally demonstrate, also as a proof-of-concept, nonlinear excitation phenomena of ROIs at micrometric scale. In particular, we show that our CIM can generate simultaneous and controllable second harmonic signal within a selected ROI. The chosen complex illumination pattern is made up of a uniform amplitude and a proper phase able to compensate few optical aberrations found at the sample plane. This phase was determined as the conjugated of that one obtained with a Shack–Hartmann wavefront sensor after sending a matrix of zero radians to the SLM. The wavefront sensor is placed at the same plane of the camera with the help of an additional beam splitter (not shown in Fig. 1). The ROI resembles again the structure of the eye of a Daphnia (similar to that shown in top part of Fig. 3). In addition, to compare the proposed CIM with a well-established illumination method, we include in the optical setup a delay line for synthetizing similar amplitude illumination patterns by means of CGHs. For this purpose the optical setup is designed such that the reconstructed CGH appears at the same distance from the lens L_3 as the complex field $U(x, y)$ does. The CGHs were designed following the Gerchberg–Saxton IFTA [21], developed in two different stages. In the first stage we perform iterations by applying only phase freedom, while the second stage the phase quantization of the hologram is softly restricted until the desired number of phase levels is reached. The algorithm converges when the result of the iteration improves the RMSE by an amount of 10^{-8}, compared with the previous one. In the experiment, we put a BBO crystal with dimensions 5 mm × 5 mm × 0.02 mm at the sample plane, as shown in Fig. 1. The unconverted infrared wavelengths of the ultrashort laser pulse were conveniently filtered with a BG39-Schott crystal before the CCD camera.

At this point, we focus our attention on irradiance rather than phase of the encoded complex field. Hence, in the left part of Fig. 5, we show only the experimental irradiance patterns reconstructed at the sample plane with the two different illumination methods. These patterns were recorded with the camera located at the position shown in Fig. 1, before placing the BBO crystal at the sample plane. From the visual comparison of both images, differences among

Optics EXPRESS

them are apparent. The reconstructed CGH roughly approximates the expected uniform irradiance pattern. Its failed attempt to reproduce a uniform illumination pattern is limited to a clear reinforcement of light at the borders of the ROI, together with the presence of coherent noise. In contrast, the irradiance pattern obtained with our CIM is almost fully flat and free from speckle noise. To better illustrate the differences between both patterns we show the irradiance profile along the central part of the ROIs. The calculated fluctuations with respect to the ideal flat profile are 62% for the CGH method, against 12% for the CIM.

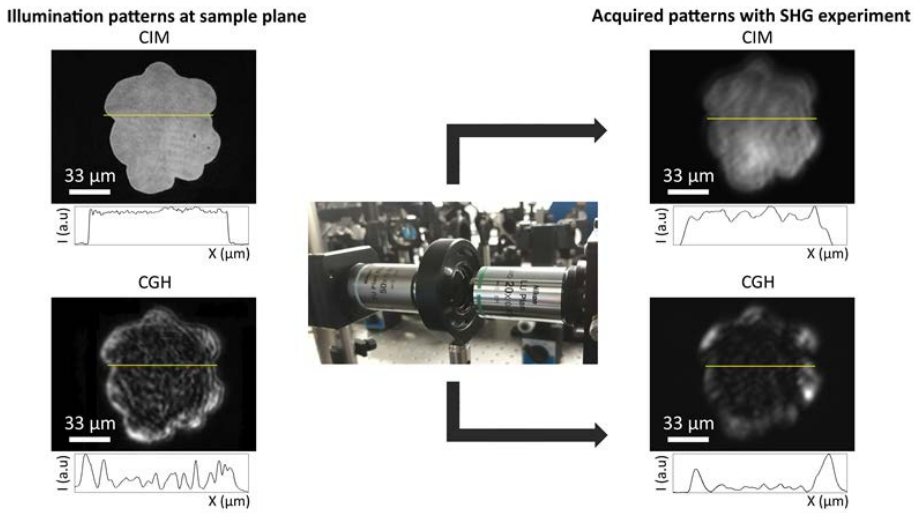

Fig. 5. Experimental images of second harmonic emission from a Daphnia 'eye ROI after employed both CGHs and our illumination method. Scales and central irradiance profiles are included as insets at the left-bottom and right-bottom parts of each irradiance pattern, respectively.

Once the nonlinear medium is placed at the focal plane, we are able to measure second harmonic signal. The corresponding recorded normalized images are shown now in the right part of Fig. 5. As it might be expected, the nonlinear response recorded in this experiment is highly dependent on the degree of flatness of the illumination patterns. That is, second harmonic image due to the illumination with reconstructed CGHs shows almost no light at those sites different from the edges of the ROI. For completeness, we include at the bottom part of each image a spatial profile of these patterns, taken again at the center of each one. This time the fluctuations with respect to the ideal flat profile are 77% for the CGH method, and 23% for the CIM.

Last experiments will be aimed to demonstrate how important could the phase control be in nonlinear excitation of ROIs when using the proposed CIM. With this purpose, we select two adjacent and micrometric ROIs located within the Daphnia's eye, which might correspond with different biological tissues in the eye. Then, we excite SHG at both ROIs, simultaneously. In these conditions, after light propagation from the sample plane to a given arbitrary defocusing plane, interference pattern dependence on the phase shift between ROIs can appear [27]. With the help of the CIM, arbitrary phase values can be easily set at different ROIs. For instance, in Fig. 6 we show four images recorded after encoding (only into one of the two ROIs) the phase values 0, $\pi/2$, π, and $3\pi/2$ radians, respectively. For this example, the selected defocusing plane was located 115 mm away from the sample plane. The recorded images shown in Fig. 6 indicate the existence of interference patterns whose structure depends on the phase shift between ROIs. Main differences among interference patterns are seen near the border of the two adjacent ROIs where the light is coherent mixed.

Optics EXPRESS

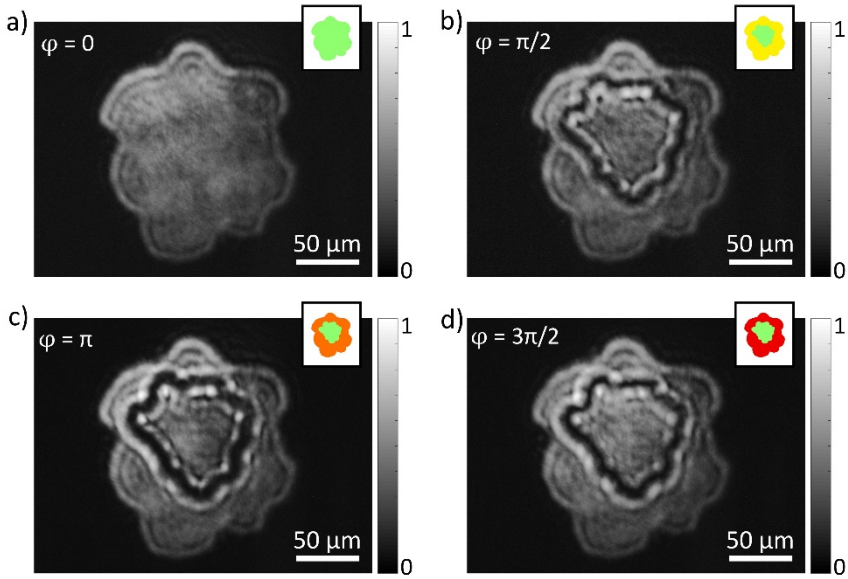

Fig. 6. Interference pattern dependence on the phase set at one ROI. The spatial shape of the selected ROIs are indicated with different colors and included as insets at the right-top part of each image.

To avoid interference border effects, we carried out a complementary experiment. This time the selected micrometric ROIs are isolated by a black surrounding ring between them such that, at the image plane, they do not interfere at all, see the right-top part of Fig. 7. To help light propagating from both ROIs to interfere, an additional convergent lens of 100 mm focal length was placed after the image plane. The position of the camera was set at an arbitrary defocusing z-axis plane located 140 mm after the Fourier plane of the added lens. In these conditions, we measured a sequence of defocusing images, each one corresponding to the setting (by means of the CIM) of a different phase value (from 0 to 2π) at one ROI, while keeping the phase at the other ROI unchanged. With all recorded images we made a movie of the evolution of the interference pattern as the phase at one ROI is increased, please see Fig. 7. Now, after watching the movie one can corroborate the presence of clear interference fringes at the previously-defined black surrounding ring. In addition, one can realize that the spatial location of these fringes depends on the phase shift between ROIs.

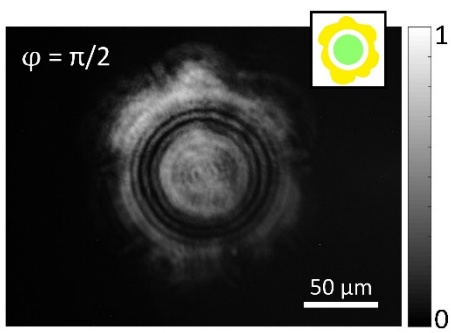

Fig. 7. Defocusing image after exciting SHG from two micrometric and separated ROIs with a set phase shift between them. The spatial shape of the selected ROIs are indicated with different colors and included as insets at the right-top part of the image. The light propagating from the ROIs interacts with one another and generates interference fringes (see Visualization 1).

Optics EXPRESS

From a practical point of view, last two experiments suggest that recorded SHG interference patterns might give us information on the relative phase between ROIs in real biological samples. Therefore, in addition to amplitude modulation, the ability of the CIM to manipulate the phase at the selected ROIs allows for practical benefits (e.g., optical aberration corrections, reduction of zero order light, or interferometric-based phase information retrieval).

5. General considerations

In this section we will discuss on significant practical issues of the CIM. For instance, in order to highly mitigate the effect of non-diffracted light (zero order) onto the sample plane, the light in the ODM enters the microscope objective MO_1 under low-focusing, instead of typical plane-wave configuration. In this way, non-diffracted light exits the microscope objective parallel to the optical axis without forming any potentially-dangerous focus near the output plane of the 4f optical system (sample plane). Hence, at the sample plane the excitation pattern is determined by the light diffracted at the SLM and the zero-order contribution. At this point, we measured the average power at the sample plane after encoding a uniform circular amplitude pattern with and without a blazed grating (with maximum grating efficiency of 80% at the first diffraction order when is codified with 4 discrete phase levels). This allows us to estimate the ratio between non-diffracted and diffracted light in the current on-axis optical arrangement. Specifically, we found a ratio of 41%. Obviously, for an off-axis optical arrangement, the zero order light can be almost completely eliminated from the sample plane with the encoding of a proper blazed grating, together with the desired complex field. The same procedure was repeated employing a holographic scheme. This time we found a ratio of 44%. In addition, thanks to the use of a long-distance focal length achromatic lens to direct the light into the microscope objective MO_1, the effects of spherical aberration at the sample plane can be disregarded. Perhaps, this can be better understood in terms of the produced Rayleigh range inside the microscope objective, which is longer and longer as far as we increase the focal length of above-mentioned achromatic lens.

Now we analyze the efficiency of the CIM. In general the efficiency of a method based on encoding information onto a SLM depends on several factors, including but not limited to technical specifications of the SLM, the type of information (amplitude or phase) that one needs to encode, characteristics of the light source, and/or the orientation of the SLM with respect to the incident light (oblique or straight light incident). In the proposed illumination method main energy losses come from the diffraction of light at the phase element, as well as due to the physical specifications of our SLM (in accordance with the manufacturer: 80% diffraction efficiency, 65-95% reflectivity, 93% fill factor, so the total light efficiency can be more than 50%). Another important issue to consider here is the size of the encoding patterns, which is directly proportional to the efficiency of the method. In other words, as in our illumination method the SLM plane is (except for the spatial filtering process) conjugated to the sample plane, an increase in the area of the encoded pattern at the SLM leads to more available light for illumination purposes. In this context, we measured the efficiency of the illumination method for the generation of irradiance patterns with the spatial shape of circumferences having different radii, and compared these results with similar ones obtained from the reconstruction of CGHs with equal shapes. To do that, we calculate the ratio of the average laser beam powers measured at the output plane of the CFEM and before the SLM with the help of a power meter (GENTEC Tuner). Our results confirm that, apart from common energy losses, the efficiency of our method is pattern-size dependent. For instance, when the encoded pattern utilizes less than 10% of the active area (about 133 mm^2) of the SLM, the classical CGH-based illumination method is more efficient than ours (for instance for encoded pattern dimensions of about 8 mm^2, we get 18% efficiency against 23% of the classical method). In contrast, when encoded patterns fill out areas greater than 25% of the SLM display area which is perhaps a more useful scenario from an energy point of view, the efficiency of

our method exceeds that of the classical one. For instance for encoded pattern dimensions of about 60 mm^2, we get 32% efficiency of our method against 23% of the classical one.

Another important point of the CIM is its potential to perform wide-field illumination and nonlinear excitation of biological samples without damage of optical components. On this aspect, the critical component of the ODM is clearly the microscope objective MO_1 that is working under low but focusing incident light conditions. The use of long-distance focal lengths certainly allows light energy inside the microcopy objective to be axially distributed along the associated Rayleigh range, decreasing in this way potential optical damage in comparison with the use of shorter focal length lenses. We measured the threshold average beam power at which nonlinear effects appear in the microscope objective. This value was about 20 mW, which turned out to be relative far from the typical average powers (4-10 mW) that we use in our experiments.

Finally we discuss on the dispersion compensation capabilities of the CIM. In the propagation of ultrashort pulses, even through non-dispersive media, there is a coupling of spatial and temporal effects due to the wavelength dependence of the diffraction integral. However, for the propagation between input and output planes of image systems (as the ones reported in this manuscript), the diffraction integral is no longer wavelength dependent and consequently, the spatiotemporal coupling no longer exists. All the distortions that appear at the output plane of our system will be just the ones introduced by the optical components, but not by the diffraction itself. So, in first order approximation, the distortions in the spectral phase of the ultrashort pulse can be pre-compensated with a common dispersion compensation module. In our case, we employed a commercially available module (Dazzler) installed in the amplification stage of our femtosecond laser. For instance, temporal pulse stretching is mainly mitigated with a proper combination of second and third order terms if we look at the maximum second harmonic signal of a BBO crystal at the sample plane. Additionally, when necessary, optical aberrations at the sample plane can also be partially compensated by encoding a suited phase mask (made up of a set of weighted aberration Zernike polynomials) together with phase element $\alpha(x, y)$ given in Eq. (4). Note that, the lack of significant dispersion contributions at the sample plane can be regarded as an advantage of our proposal in comparison with other illumination strategies e.g., CGHs.

6. Conclusions

In this manuscript we have proposed and tested an interferometric CIM mainly addressed to microscopy applications which is able to achieve simultaneous linear and/or non-linear excitation of user-defined ROIs. The introduced CIM provides not only full control over the amplitude and phase of the complex field at the sample plane, but also reduces speckled noise due to the use of coherent illumination sources. The complex illumination pattern is basically generated from a single phase element (calculated from the double-phase hologram theory) and encoded into a phase-only SLM. In the optical setup made up of a couple of modules called CFEM and ODM, the light coming from the SLM is spatially filtered and demagnified with proper optical components before arriving to the sample plane.

In the manuscript we have discussed both the theory underlying the CIM as well as its experimental performance, including zero order behavior, dispersion compensation capabilities or efficiency. In practice, the proposed CIM has been validated with several experiments aimed to produce linear and non-linear excitation of specific ROIs with user-defined complex illumination patterns. In addition some benefits of our CIM over other illumination schemes based on IFTAs and implemented with phase-only SLMs have been highlighted with practical demonstrations related to aberration compensation or interferometric-based phase information retrieval tasks.

Our experiments show that in principle, under fully controllable amplitude and phase parameters, not only linear but also second harmonic excitation of different ROIs at

micrometric scale is feasible. Here, it should be mentioned that these experiments can only be considered as a proof-of-concept. It is apparent that additional tests must be done in order to validate the proposed CIM i.e., use it as the illumination path of a commercial microscope and/or by studying its behavior under real biological samples. However, we do believe that achieved results should be enough to show the potential of the proposed CIM for microscopy applications. For instance, the probed ability of the CIM to simultaneous excite spatially-extended ROIs and simultaneously compensate for optical aberrations might positively contribute to decrease the acquisition time and/or improve the spatial resolution of acquired images. To this end, a proper combination of the proposed CIM with high-sensitivity cameras is expected. Moreover, to enhance axial resolution, CIM can be combined with well-known temporal focusing methods [8,20].

Funding

Generalitat Valenciana (AICO/2016/036, PROMETEO 2016-079); Universitat Jaume I (UJI) (UJIB2016-19); Ministerio de Economía y Competitividad (MINECO) (FIS2016-75618-R).

Acknowledgments

The authors are very grateful to the SCIC of the Universitat Jaume I for the use of the femtosecond laser.

References

1. C. K. Kim, S. J. Yang, N. Pichamoorthy, N. P. Young, I. Kauvar, J. H. Jennings, T. N. Lerner, A. Berndt, S. Y. Lee, C. Ramakrishnan, T. J. Davidson, M. Inoue, H. Bito, and K. Deisseroth, "Simultaneous fast measurement of circuit dynamics at multiple sites across the mammalian brain," Nat. Methods **13**(4), 325–328 (2016).
2. M. Ducros, Y. Goulam Houssen, J. Bradley, V. de Sars, and S. Charpak, "Encoded multisite two-photon microscopy," Proc. Natl. Acad. Sci. U.S.A. **110**(32), 13138–13143 (2013).
3. M. T. Butko, M. Drobizhev, N. S. Makarov, A. Rebane, B. C. Brinkman, and J. G. Gleeson, "Simultaneous multiple-excitation multiphoton microscopy yields increased imaging sensitivity and specificity," BMC Biotechnol. **11**(1), 20 (2011).
4. M. Ingaramo, A. G. York, P. Wawrzusin, O. Milberg, A. Hong, R. Weigert, H. Shroff, and G. H. Patterson, "Two-photon excitation improves multifocal structured illumination microscopy in thick scattering tissue," Proc. Natl. Acad. Sci. U.S.A. **111**(14), 5254–5259 (2014).
5. A. Egner and S. W. Hell, "Time multiplexing and parallelization in multifocal multiphoton microscopy," J. Opt. Soc. Am. A **17**(7), 1192–1201 (2000).
6. S. Lévêque-Fort, M. P. Fontaine-Aupart, G. Roger, and P. Georges, "Fluorescence-lifetime imaging with a multifocal two-photon microscope," Opt. Lett. **29**(24), 2884–2886 (2004).
7. E. Papagiakoumou, V. de Sars, D. Oron, and V. Emiliani, "Patterned two-photon illumination by spatiotemporal shaping of ultrashort pulses," Opt. Express **16**(26), 22039–22047 (2008).
8. L.-C. Cheng, C.-Y. Chang, C.-Y. Lin, K.-C. Cho, W.-C. Yen, N.-S. Chang, C. Xu, C. Y. Dong, and S.-J. Chen, "Spatiotemporal focusing-based widefield multiphoton microscopy for fast optical sectioning," Opt. Express **20**(8), 8939–8948 (2012).
9. M. D. Peterson, P. L. Hayes, I. S. Martinez, L. C. Cass, J. L. Achtyl, E. A. Weiss, and F. M. Geiger, "Second harmonic generation imaging with a kHz amplifier [Invited]," Opt. Mater. Express **1**(1), 57–66 (2011).
10. V. Nikolenko, D. S. Peterka, R. Araya, A. Woodruff, and R. Yuste, "Spatial light modulator microscopy," Cold Spring Harb. Protoc. **2013**(12), 1132–1141 (2013).
11. Y. Hertzberg, O. Naor, A. Volovick, and S. Shoham, "Towards multifocal ultrasonic neural stimulation: pattern generation algorithms," J. Neural Eng. **7**(5), 056002 (2010).
12. O. Mendoza-Yero, G. Mínguez-Vega, and J. Lancis, "Encoding complex fields by using a phase-only optical element," Opt. Lett. **39**(7), 1740–1743 (2014).
13. E. Papagiakoumou, F. Anselmi, A. Bègue, V. de Sars, J. Glückstad, E. Y. Isacoff, and V. Emiliani, "Scanless two-photon excitation of channelrhodopsin-2," Nat. Methods **7**(10), 848–854 (2010).
14. I. Pastirk, J. Dela Cruz, K. Walowicz, V. Lozovoy, and M. Dantus, "Selective two-photon microscopy with shaped femtosecond pulses," Opt. Express **11**(14), 1695–1701 (2003).
15. C. Maurer, A. Jesacher, S. Bernet, and M. Ritsch-Marte, "What spatial light modulators can do for optical microscopy," Laser Photonics Rev. **5**(1), 81–101 (2011).
16. S. Bovetti and T. Fellin, "Optical dissection of brain circuits with patterned illumination through the phase modulation of light," J. Neurosci. Methods **241**, 66–77 (2015).
17. D. Tanese, J.-Y. Weng, V. Zampini, V. De Sars, M. Canepari, B. Rozsa, V. Emiliani, and D. Zecevic, "Imaging membrane potential changes from dendritic spines using computer-generated holography," Neurophotonics **4**(3), 031211 (2017).

Optics EXPRESS

18. A. Jesacher, C. Maurer, A. Schwaighofer, S. Bernet, and M. Ritsch-Marte, "Near-perfect hologram reconstruction with a spatial light modulator," Opt. Express **16**(4), 2597–2603 (2008).
19. S. J. Yang, W. E. Allen, I. Kauvar, A. S. Andalman, N. P. Young, C. K. Kim, J. H. Marshel, G. Wetzstein, and K. Deisseroth, "Extended field-of-view and increased-signal 3D holographic illumination with time-division multiplexing," Opt. Express **23**(25), 32573–32581 (2015).
20. N. Accanto, C. Molinier, D. Tanese, E. Ronzitti, Z. L. Newman, C. Wyart, E. Isacoff, E. Papagiakoumou, and V. Emiliani, "Multiplexed temporally focused light shaping for high-resolution multi-cell targeting," Optica **5**(11), 1478–1491 (2018).
21. R. W. Gerchberg and W. O. Saxton, "A practical algorithm for the determination of phase from image and diffraction plane pictures," Optik (Stuttg.) **35**(2), 237–246 (1972).
22. T. Aharoni and S. Shoham, "Phase-controlled, speckle-free holographic projection with applications in precision optogenetics," Neurophotonics **5**(2), 025004 (2018).
23. R. Conti, O. Assayag, V. de Sars, M. Guillon, and V. Emiliani, "Computer generated holography with intensity-graded patterns," Front. Cell. Neurosci. **10**, 236 (2016).
24. O. Mendoza-Yero, G. Minguez-Vega, L. Martinez-Leon, M. Carbonell-Leal, M. Fernandez-Alonso, C. Donate-Buendia, J. Perez-Vizcaino, and J. Lancis, "Diffraction-based phase calibration of spatial light modulators with binary phase Fresnel lenses," J. Disp. Technol. **12**(10), 1027–1032 (2016).
25. M. Persson, D. Engström, and M. Goksör, "Reducing the effect of pixel crosstalk in phase only spatial light modulators," Opt. Express **20**(20), 22334–22343 (2012).
26. I. Yamaguchi and T. Zhang, "Phase-shifting digital holography," Opt. Lett. **22**(16), 1268–1270 (1997).
27. R. Bäumner, L. Bonacina, J. Enderlein, J. Extermann, T. Fricke-Begemann, G. Marowsky, and J. P. Wolf, "Evanescent-field-induced second harmonic generation by noncentrosymmetric nanoparticles," Opt. Express **18**(22), 23218–23225 (2010).